Microfluidic Pump Driven by Anisotropic Phoresis

Zihan Tan,[1,2,*] Mingcheng Yang,[3,4,†] and Marisol Ripoll[1,‡]

[1] *Theoretical Soft-Matter and Biophysics, Institute of Complex Systems, Forschungszentrum Jülich, Jülich 52425, Germany*

[2] *Soft Condensed Matter, Institute of Complex Systems, Forschungszentrum Jülich, 52425 Jülich, Germany*

[3] *Beijing National Laboratory for Condensed Matter Physics and Key Laboratory of Soft Matter Physics, Institute of Physics, Chinese Academy of Sciences, Beijing 100190, China*

[4] *University of Chinese Academy of Sciences, Beijing 100049, China*

Fluid flow along microchannels can be induced by keeping opposite walls at different temperatures and placing elongated tilted pillars inside the channel. The driving force for this fluid motion arises from the anisotropic thermophoretic effect of the elongated pillars that generates a force parallel to the walls and perpendicular to the temperature gradient. The force is not determined by the thermophilic or thermophobic character of the obstacle surface, but by the geometry and the thermophoretic anisotropy of the obstacle. Via mesoscale hydrodynamic simulations, we investigate the pumping properties of the device as a function of the channel geometry and pillar surface properties. Applications as fluidic mixers and fluid alternators are also outlined, together with the potential use of all these devices to harvest waste heat energy. Furthermore, similar devices can also be built employing diffusiophoresis or electrophoresis.

I. INTRODUCTION

Guiding the movement of fluid at nano- and microscales has become one of the most challenging goals in the emergent field of microfluidics [1,2]. Relevant applications of microfluid pumping are related with drug delivery [3,4], biomedical assays [5,6], and cell culturing [7]. An efficient microfluidic pump requires the capability to use minimal quantities of energy to carry fluid with high resolution and sensitivity. In microfluidic devices, fluids are typically transported, separated, or processed along microchannels of different compositions and geometries. The generation of net fluid flows is frequently achieved by applying external mechanical forces with coupled inlet and outlet systems [8–10]. The efficiency of such driving mechanisms importantly decreases with miniaturization because of the huge increase in hydrodynamic resistance that comes with downsizing [11]. Moreover, the fact that inlets and outlets rely on external pieces of equipment importantly hampers the portability of the devices. A competitive approach is to induce stresses localized at the boundaries, through nonmechanical means, which are driven typically by local fields [12–16]. This has shown to be especially efficient for miniaturizing fluidic pumps, due to the intrinsically large surface-to-volume ratio.

Phoretic or the related osmotic properties of solid materials in a fluid solution constitute an attractive option to induce stresses close to confining walls. Phoresis refers to the directed drift motion of a suspended particle induced due to an inhomogeneous surrounding [17,18], which can be, for example, a temperature gradient (thermophoresis) [19–22], a concentration gradient (diffusiophoresis) [23–25], or an electric potential gradient (electrophoresis) [26–28]. Conversely, the gradient can generate the motion of a fluid at a fixed solid-fluid interface, which is usually referred to as phoretic osmosis, and in the case of a fluid-fluid interface, which is known as a phoretic capillary [17]. Catalytic surfaces and related chemical gradients have shown a large potential in microfluidic applications [29–32], while thermal gradients are relatively less exploited. Thermal gradient-driven motion has, however, promising prospects, since it works equally well in charged and neutral solutions and it is pollution free due to the absence of surfactants or chemical fuels, which enormously facilitates biocompatible applications [33–35]. Furthermore, thermal gradient-driven motion allows optical microscale operations with optical heating, which is the basic principle of the emerging field of optofluidics [36,37]. So far, existing phoretic fluidics relies on intricate differentiated compositions [38–40] or ratchet geometries of channel walls [14,41–43]. To extend the tunability and functionality of these pumps is therefore timely and highly desirable.

_____

*z.tan@fz-juelich.de

†mcyang@iphy.ac.cn

‡m.ripoll@fz-juelich.de

Anisotropic thermophoresis has been recently described and open a new avenue for the design of novel and versatile microdevices [44,45]. The anisotropic phoretic effect refers to the different phoretic response that elongated objects, such as colloids or pillars, have when aligned with or perpendicular to the external gradient. Interestingly, for obstacles with tilted orientation, this anisotropy might translate into a force that would not only be aligned with the gradient, as it is in the case of traditional phoresis, but additionally also perpendicular to the gradient. This mechanism has already been employed for the design of microturbines that can rotate unidirectionally [45]. Given the related nature of different phoretic effects, this effect has been proved to exist not only for thermophoresis, but also for diffusiophoresis, for example, in the presence of multicomponent fluids with catalytic surfaces [46].

In this work, we propose a class of microfluidic pumps based on the anisotropic phoretic effect. Instead of considering the asymmetries at the channel walls as in previous devices, we present a micropump exploiting the tunable properties of the immersed solid obstacles with thermophoretic anisotropy in the middle of the channel, which could be engineered, for example, by means of lithography [47,48]. Opposite walls have fixed different temperatures, such that the pillars are exposed to a temperature gradient. The phoretic properties of the pillars' surface thus generates a fluid flow along the microchannel, perpendicular to the thermal gradient. The device will have a large versatility due to factors intrinsic to the pump, such as the pillars' geometry; number of obstacles per unit length; obstacles' configuration; or the subtle dependence of the phoretic behavior on a large number of factors such as average temperature or pressure, presence of salt, or surface coatings, among many others. Also, very remarkable will be the case in which the obstacles do not have a fixed orientation with respect to the walls, but can be externally controlled *in situ*, e.g., by laser tweezers on suspended colloids, such that the flow pattern becomes highly adjustable and rich. In addition, the suspended objects may even be removed from and imported into the channel without affecting the channel itself. Furthermore, variations of the microchannel device are shown to work not only as microfluidic pumps with arbitrarily microchannel length, but also as fluidic mixers or generators of alternating flow. Finally, given the fact that they work under the effect of external gradients, they all have potential applications to harvest waste thermal or chemical energy.

II. MODEL AND MECHANISM

A. Simulation setup

Simulations are performed with a mesoscale hydrodynamic approach, which combines multiple particle collision dynamics (MPC) and molecular dynamics (MD) [49–52]. MPC is a particle-based model in which a coarse-grain solvent is represented by N point particles of mass m, characterized by continuous positions $\mathbf{r}_i$ and velocities $\mathbf{v}_i$ ($i = 1, \ldots, N$), which evolve in two alternating steps. In the streaming step, particle positions evolve ballistically for a certain time h, which we refer to as the "collision time." In the collision step, particles are sorted into cubic cells, with cell size a, and each particle rotates its relative velocity to the cell center of mass velocity by an angle α around a randomly chosen direction. The collisional operation conserves mass, linear momentum, and energy at the cell level. The cell grid is randomly displaced to maintain Galilean invariance [53] and enhance the fluidlike properties of the solvent [54–56]. Standard simulation units are chosen, $m = k_B T = a = 1$, with $k_B T$ the averaged temperature, which means, for example, that time is given in units of $\sqrt{ma^2/(k_B T)}$, which is typically not specified. The usual MPC parameters are used, $h = 0.1$, $\alpha = 130°$, and $\rho = 10$ average number of particles per collision box, corresponding to a kinematic viscosity $\nu = 0.87$. For the direct comparison with real fluids, dimensionless numbers are typically calculated, such as the Schmidt number Sc or the Prandlt number Pr, which for the specified parameters are Sc $= 17$ and Pr $= 5.8$ respectively. In this respect, Pr shows to be very close to most relevant fluids such as water, although Sc is clearly smaller. While the Prandlt number indicates that the transport of heat and momentum is properly separated in our case, the Schmidt number refers to the separation of mass and momentum, which, in our case, are less separated than in most fluids. This lower value might be an issue when quantitatively mapping to real units, although it is absolutely not a problem to reproduce a fluid with correct liquidlike dynamics [56,57]. Solid channel walls with stick boundary conditions are realized by applying the bounce-back rule to the solvent particles when reaching the walls, and the temperature gradient is implemented by thermostatting thin solvent layers close to the walls with low T_c and high T_h temperatures [58,59]. The employed default temperatures at the no-slip walls are $T_h = 1.2$ and $T_c = 0.8$ in MPC units. These could be converted to real units by considering, for example, an average temperature equal to $T = 300$ K, corresponding to very high temperature differences, although, as later discussed, this could be compensated with other unit mismatches.

The thermophoretic micropump, sketched in Figs. 1(a) and 1(b), consists of a microchannel of width H with immersed solid elongated obstacles (pillars) tilted at an angle θ, typically $\theta = 45°$. Opposite walls have fixed different temperatures, such that the pillars feel a temperature gradient ∇T, which induces an osmotic flow. As indicated in Fig. 1(c), pillars are modeled by one layer of spherical beads of the diameter d, fixed in this work to $d = 2.5a$, placed with anchored positions on the nodes of a triangular lattice. The separation between beads determines the pillar surface rugosity, which is characterized by the ratio between the typical lattice length l and the bead diameter d.
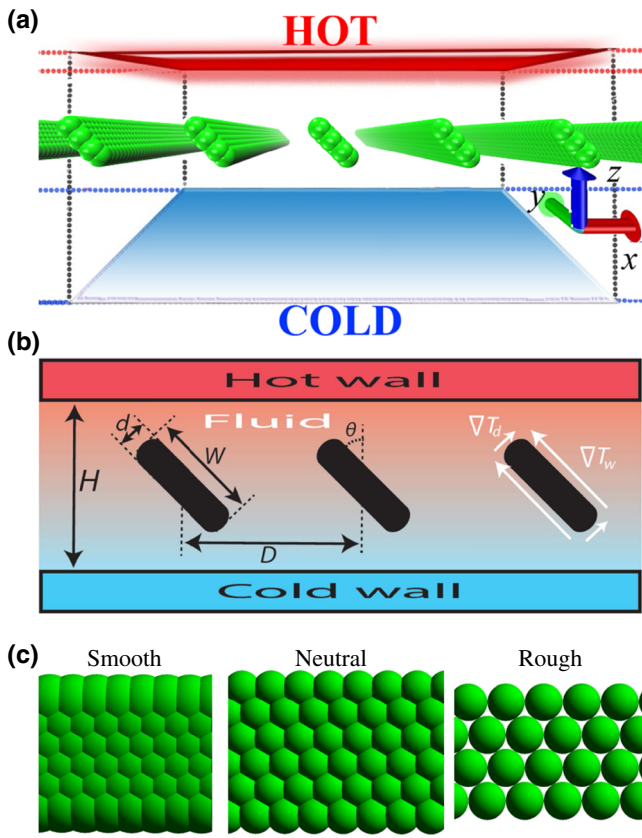
FIG. 1. (a) Sketch of the anisotropic micropump, composed by two planar walls at fixed different temperatures, with solid elongated titled obstacles. (b) Cross-section sketch of the relevant device dimensions. The channel width is H, each pillar has a length W and thickness d, and multiple obstacles are separated by a distance D. The temperature gradients along the long and short axes are ∇T_d and ∇T_W. (c) Detailed structure of pillars with rugosities $l/d = 0.4$, 0.8, and 1, referred to as smooth, neutral, and rough.

In this way, small values such as $l/d = 0.4$ are referred to as smooth surfaces, while large values such as $l/d = 1$ are referred to as rough. In order to modify the surface thermophoretic properties, the rugosity is here modified similar to the rodlike colloid case. The rough case corresponds then to porouslike material where fluid can cross through the pillars' interstices. The pillar thickness is for all rugosities, the particle diameter d, and the length is denoted by W, which is typically not an integer given the varying values of the rugosity. Periodic boundary conditions (PBC) are considered in the two directions perpendicular to the walls. Pillars are placed with the long axis parallel to the walls; this is in the y direction as depicted in Fig. 1(a). This, together with PBC, provides effective extended pillars. Finally, the pillars are equidistantly placed in the x direction, with separation D. Unless otherwise stated, we perform simulations with $l/d = 0.4$, $W = 2.93d$, $D = H = 12d$, and with one obstacle in a cuboid box $(L_x, L_y, H) = (30, 20, 30)$. The beads' positions are invariable with time,

and the interaction of the solvent particles with the pillar beads is modeled by the Mie potential [60] (namely, the Lennard-Jones type)

$$U(r) = 4\epsilon \left[\left(\frac{d}{2r} \right)^{2n} - \left(\frac{d}{2r} \right)^{n} \right] + c, \quad r \le r_c. \quad (1)$$

Here, r is the distance between the bead center and the fluid particle; ϵ is the potential intensity, chosen as $\epsilon = k_B T$; and n is a positive integer describing the potential stiffness. By considering $c = 0$ or $c = \epsilon$ together with the suitable cutoff distance r_c, the potential is adjusted to be attractive or purely repulsive [61], which is respectively denoted as *an* or *rn*. This means, for example, that the *r*6 potential with $n = 6$, $c = \epsilon$, and $r_c = 2^{1/6}d$ is the well-known Weeks-Anderson-Chandler (WAC) repulsive potential [62].

B. Mechanism: anisotropic thermophoresis

The interaction of a colloidal particle with a solvent with a nonhomogeneous temperature results in a driving thermophoretic force $\mathbf{F}_T$ [63,64], which causes the particle migration of nonfixed particles (thermophoresis) or the motion of the surrounding fluid for immobilized objects (thermoosmosis). This force is known to be directly proportional to the temperature gradient,

$$\mathbf{F}_T = -\Lambda_T \cdot k_B \nabla T, \quad (2)$$

with k_B the Boltzmann constant and Λ_T the thermodiffusion tensor, which is a material-dependent property determining the force direction and strength. In the case of spherical particles, Λ_T is a constant factor, the so-called "thermodiffusion factor," α_T, while other particle shapes might have more complex dependencies. This deviation from the spherical constant behavior has been defined as "anisotropic thermophoresis" [44]. In the case of elongated particles, two independent coefficients are expected to be enough to determine the thermophoretic properties. These are $\alpha_{T,\parallel}$ and $\alpha_{T,\perp}$, the thermophoretic factors characterizing a rod with the long axis aligned with the temperature gradient or perpendicular to it. The difference between these two factors defines the thermophoretic anisotropy factor

$$\chi_T = \alpha_{T,\perp} - \alpha_{T,\parallel}. \quad (3)$$

Interestingly, this means that an elongated particle with $\chi_T \neq 0$ fixed at an angle θ with respect to ∇T feels a force not only in the gradient direction, but also perpendicular to it, as follows (Due to the system geometry, note that the angle θ here has opposite orientation as in [44,45]):

$$\mathbf{F}_{T,x} = -\chi_T \sin\theta \cos\theta k_B |\nabla T| \mathbf{e}_x, \quad (4)$$

where x refers to the direction perpendicular to ∇T and $\mathbf{e}_x$ the corresponding unit vector. By convention, the sign
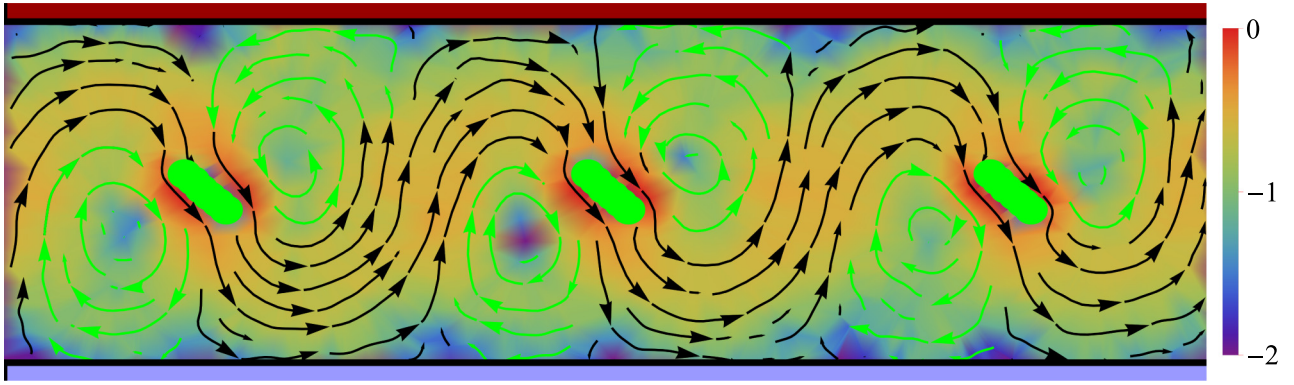
FIG. 2. Flow streamlines corresponding to the micropump in Fig. 1(b). Here and in what follows, the background color codes the magnitude of local velocities $|\mathbf{v}(x,z)|$ rescaled with a factor of $\log(|\mathbf{v}| - |\mathbf{v}|_{min}) / \log(|\mathbf{v}|_{max} - |\mathbf{v}|_{min})$, where $|\mathbf{v}|_{max}$ and $|\mathbf{v}|_{min}$ are the maximum and minimum of magnitudes of the velocities in each vector field. As a guide to the eye, black lines correspond to the net flow and green lines to the vortices.

of the thermodiffusion factor α_T is positive when colloids drift toward cold areas (thermophobic behavior), while α_T is negative for colloids drifting toward warmer areas (thermophilic behavior). Previous simulations showed that the use of attractive solvent-colloid potentials translates into a thermophobic colloid drift, while repulsive potentials show a thermophobic behavior. This driven mechanism of the model is essentially related to the relation between the local pressure gradient and the sign of the applied potential [65,66]. The direction of the perpendicular force $F_{T,x}$ in Eq. (4) is determined by the sign of χ_T, which is, in principle, independent of the thermophobic or thermophilic character of the surface.

In the microchannel configuration of Fig. 1, the fixed solid pillars endure thermo-osmotic flows of the fluid around them. If the obstacles are elongated structures ($W \neq d$), tilted with respect to the channel walls and therefore to the temperature gradient ($0° < \theta < 90°$), a net fluid flux will be generated parallel to the channel walls, as can be seen in Fig. 2. The resulting net flux density $\hat{J}$ can be defined as the particle flux per unit volume,

$$\hat{J}(x) = \frac{1}{H} \int_0^H \rho(x,z) v_x(x,z) dz, \quad (5)$$

where $\rho(x,z)$ is the average particle number and $v_x(x,z)$ the particle velocity of the fluid at the position (x,z). Note that the fluid velocity is not fully considered, but just the velocity component parallel to the walls, since this is the only one that contributes to the net flux. The system symmetry allows us to disregard the system dependence along the obstacle length, which in Fig. 1(a) corresponds to the y direction. In order to provide a prediction to the corresponding averaged density flux, it is important to note that the normalized number density can be considered proportional to ρ_0, the averaged number density; while the fluid velocity is determined by the perpendicular

thermophoretic force $\mathbf{F}_{T,x}$ in Eq. (4), together with an effective friction coefficient proportional to the fluid viscosity η. The averaged density flux is then determined by

$$\tilde{J} = G(W, D, H) \frac{\rho_0}{\eta} \chi_T k_B |\nabla T|, \quad (6)$$

where a fixed-angle inclination has already been accounted for, for example, its optimal value $\theta = \pi/4$, and $G(W, D, H)$ is a function of the microchannel and pillar geometry with the inverse of length dimensions. Expression (6) indicates that the intensity of the flux is determined by several parameters, but the direction is remarkably only determined by the anisotropic thermophoretic factor χ_T.

III. FLOW PATTERN AND FLOW FLUX

A representative simulation output of the temporally averaged flow streamlines of a cross section in the x-z plane with three pillars is illustrated in Fig. 2. This flow pattern has an "effective flow" region where the fluid passes close to the obstacles and continues along the microchannel with a sinusoidal-like trajectory. Additionally, a "vortex" region can be identified, where the flow rotates without providing any net contribution to the total flux.

The resulting net flux density $\hat{J}$ as defined in Eq. (5) is computed along the channel and displayed in Fig. 3(a), normalized by the externally applied temperature gradient. In spite of the streamline's tortuosity, and because of the mass continuity, the flux density is basically constant along the channel [see Fig. 3(a)]. Note that the flow does not depend on the position in the y axis, such that we average the flow field in this direction to increase the statistical accuracy. Both the flow field and the flux at steady state are temporally averaged over 5×10^5 units of time with at least 24 simulation measurements. Note that increasing the number of simulations would eventually improve
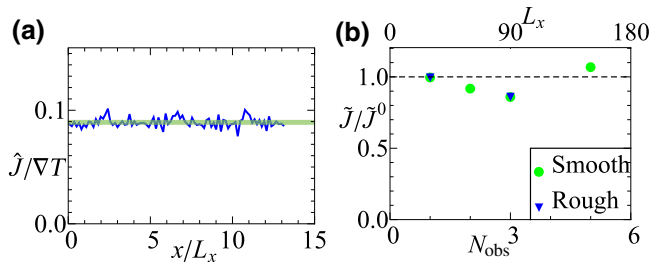
FIG. 3. (a) Scaled flux density corresponding to the setup in Fig. 2, calculated along the channel length. The green transparent line represents the average value. (b) Normalized flux density calculated with different numbers of pillars in the primary simulation box, N_{obs}, with constant obstacle separation D. $\tilde{J}^0$ is the flux density with one obstacle in the primary box, with $D = L_x$, for two different values of the pillar rugosity.

the statistical dispersion of the data and decrease the (not indicated) error bars, but it would not change any of the presented conclusions.

Given the system's symmetry and the use of PBC along the channel, the fluid flow is not expected to significantly depend on the number of pillars considered, for a fixed interparticle separation D. However, PBC might also lead to fluid correlations, which would be enhanced for smaller system sizes [67]. In Fig. 3(b), measurements of the flux densities are shown for simulations with different numbers of obstacles in the primary simulation box, N_{obs}, where the box dimension has been accordingly varied, $L_x = N_{\text{obs}}D$. The flux densities show a relatively constant value, independent of the system size, and furthermore, the flow patterns around each pillar are identical for different N_{obs}, which allows us to investigate systems with just one pillar without diminishing the applicability of the conclusions.

A. Interfacial properties

The thermophilic character of the pillar in Fig. 2 can be observed in the flow close to the obstacle surface, where the flow is clearly directed from warm to cold areas, opposite to the thermophoretic force on the pillar beads, as expected [59]. A similar micropump, with an obstacle constructed out of thermophobic beads, is displayed in Fig. 4, where the flow directed then to the warm areas can be observed in the neighborhood of the obstacle surface. In spite of this difference, the overall direction of the flux is the same in these two cases, which results in flow streamlines with significantly different pathways in both cases, as can be seen by the flow close to the pillar and the position of the stagnation point relative to the obstacle.

As stated in Eq. (6), the overall direction of the flow parallel to the walls is determined by the anisotropic factor χ_T in Eq. (3). This explains that pillars with thermophilic and thermophobic character might still result in flux with the same direction. To further verify this statement, we
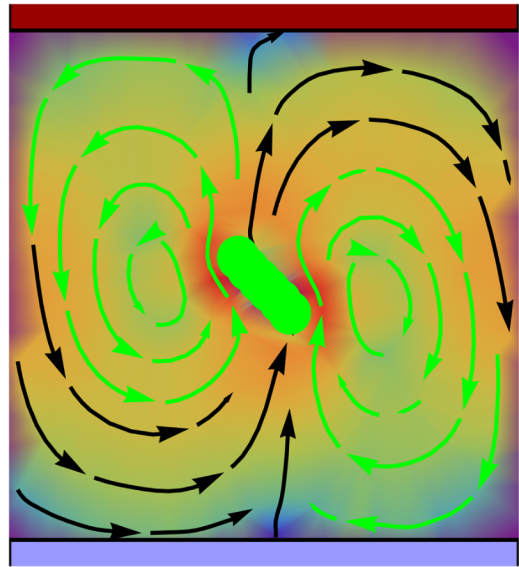

FIG. 4. Flow streamlines of a micropump with a thermophobic pillar ($a24$ potential).

quantify χ_T in some cases by additional simulations with obstacles placed parallel and perpendicular to the channel walls, using a procedure similar to the one described in Ref. [44]. Results and simulation parameters are summarized in Table I. The variation of the flux normalized by the applied temperature gradient with the corresponding anisotropic thermophoresis factor χ_T is displayed in Fig. 5, where the linear behavior predicted by Eq. (6) is nicely confirmed. Note that, in our simulations, the pillars along the y direction are constructed by PBC. Therefore, the values of χ_T are represented as the measured χ_T per unit length along the y axis.

The investigation of the anisotropic thermophoretic effect in colloidal rods [44] showed a sign change of χ_T with the rod rugosity. We also explore the dependence with rugosity in the case of elongated obstacles as depicted in Fig. 1(c), and the explicit measurements of χ_T shown in Table I display a similar sign change. The streamlines for microchannels with elongated rough and neutral thermophilic pillars are plotted in Fig. 6, while the smooth corresponding case can be seen in Fig. 2. The flux direction and the flow pathways are different in the three cases

TABLE I. Measurements of χ_T and flow fluxes $\tilde{J}$ for the simulations performed with the default geometrical dimensions, namely, $H = D = L_x = 12d$.

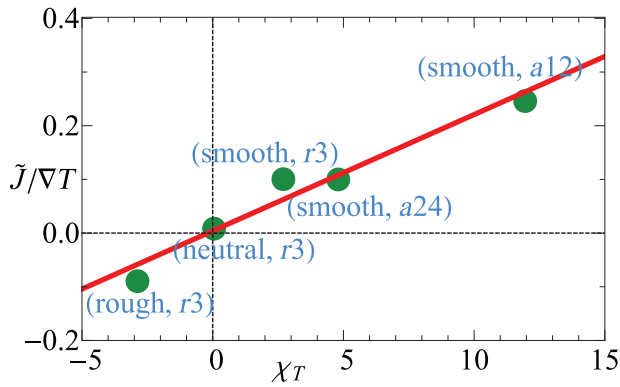| Potential	$r3$	$r3$	$r3$	$a24$	$a12$
l/d	1.0	0.8	0.4	0.4	0.4
W/d	3.60	3.08	2.93	2.93	2.93
∇T	0.0207	0.0138	0.0138	0.0172	0.0172
$\alpha_{T,\perp}$	-9	-10	-13	27	44
χ_T	-2.88	0.050	2.700	4.800	11.950
$\tilde{J}/\nabla T$	-0.086	0.011	0.104	0.103	0.249

FIG. 5. Variation of the normalized flux $\tilde{J}/\nabla T$ as a function of the anisotropic thermophoresis factor χ_T, with parameters specified in Table I. The red line corresponds to linear behavior in Eq. (6).

as a consequence of the different values of χ_T. Besides the change in flux direction, the location of the vortices and the corresponding stagnation points vary also with χ_T and the thermophoretic character. For the microchannel with smooth thermophilic obstacles (Fig. 2), this is when $|\alpha_{T,\parallel}| > |\alpha_{T,\perp}|$; the stagnation points are aligned perpendicular to the long pillar axis. On the other hand, for cases with $|\alpha_{T,\parallel}| < |\alpha_{T,\perp}|$, these are smooth thermophobic (Fig. 4) or rough thermophilic obstacles [Fig. 6(a)]; the stagnation points are aligned close to the long pillar axis. Finally, it is interesting to note that there is an intermediate rugosity case, which we call neutral, for which the anisotropic effect vanishes, $\chi_T \simeq 0$. This is the case shown in Fig. 6(b), where the flow field shows a symmetric pattern very close to the vanishing flux, which resembles the one induced by a fixed isotropic colloid [59].

B. Channel geometrical properties

Besides the interfacial properties discussed previously, the channel dimensions are naturally going to affect the
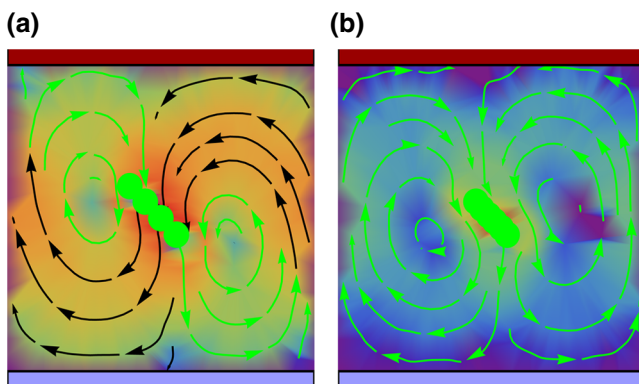
(a) **(b)**

FIG. 6. Flow fields with varying pillar surface rugosity: (a) rough obstacle surface, $l/d = 1.0$; (b) neutral obstacle surface, $l/d = 0.8$.

flow intensity, shape, and exceptionally even its sign, as indicated by the prefactor in Eq. (6) being a function of the channel width, pillar interseparation, and obstacle aspect ratio.

1. Channel width effect.

To study the effect of the channel width on the induced flow, we perform simulations varying H, from approximately 3 to 9 times the obstacle length W, and fixing all the other dimensions to default values, as well as the temperatures at the two walls ($T_h = 1.31$ and $T_c = 0.68$). Figure 7 shows the cases with the largest and smallest confinements investigated here, which can be compared with the intermediate case in Fig. 2. The confinement provided by the no-slip channel walls restricts the effective flow domain and adjusts the fluid flow perpendicular to the walls rather than parallel to them. This wall restriction of the flow explains the linear increase of the flux with channel width shown in Fig. 8(a). For channels wide enough, the flow close to the walls is weak, approximately $10^{-2} |v|_{\max}$, such that confinement no longer noticeably affects the flow, and an increase of the channel width results in a straightforward decrease of the net flux. This explains the maximum observed in Fig. 8(a) for channels with $H \simeq 7.3 W$.

Additionally, Fig. 7 shows that the channel width also importantly changes the size, shape, and location of the vortex regions, which is a consequence of the previously discussed flow distortion. The vortices can be quantitatively characterized with the location of the middle points of zero flow velocity, by defining the stagnation angle φ and the normalized stagnation distance S_d/W. As indicated in Fig. 7(a), S_d is the distance between the two stagnation points S_1 and S_2 around a given pillar and φ is the angle that the line connecting these two points makes with the pillar elongated axis. Figure 8(a) shows that both of these quantities have a maximum at the same point as the normalized flux and that this occurs when $\varphi = 90°$; this is when the vortex middle points are exactly perpendicular with the elongated obstacle. When H is as small as shown in Fig. 7(a), the vortex region takes up a large part of the microchannel due to the significant confinement in the gradient direction and the distance between complementary stagnation points is very small. The size and position of the vortex changes exactly until $\varphi = 90°$, a value from which the vortices only distort due to the lack of confinement.

The velocity profiles along the channel direction v_x in the cross sections perpendicular and parallel to the channel walls are shown in Figs. 8(c) and 8(d), respectively. Figure 8(c) shows that the velocity profile in between the obstacles is close to parabolic, with a slightly off-center maximum, in which the maximum values of the velocity follow the same dependence as the fluxes in Fig. 8(a). This means that the intensity of the flow decays close to the walls, and this decay is then larger for the widest channels
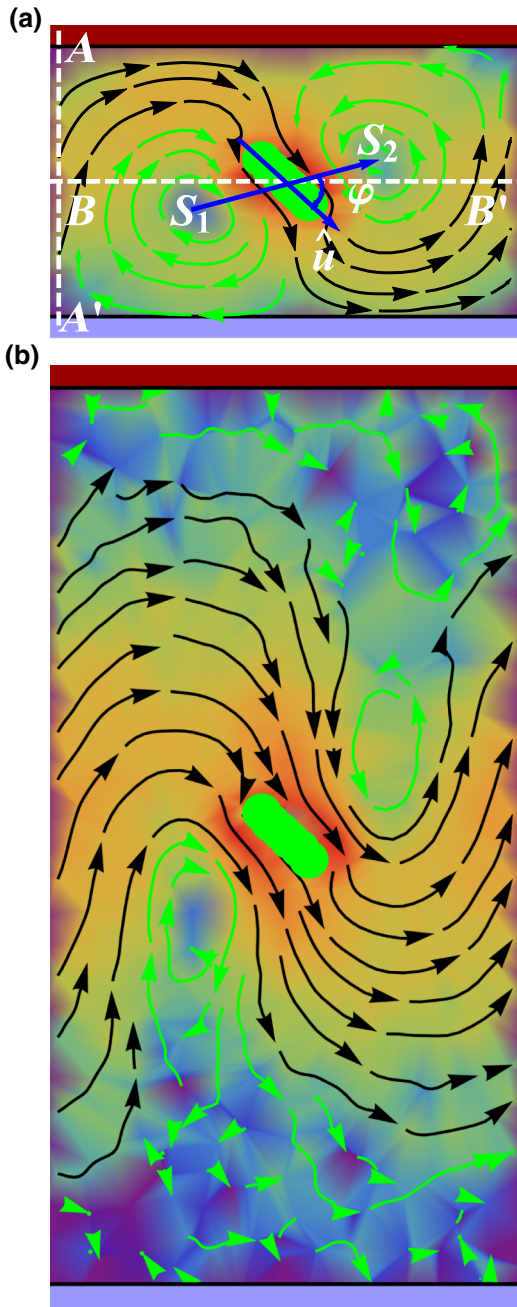
FIG. 7.   Flow field for channels of different channel widths. (a) Strongly confined case with $H = 2.93\,W$. This figure shows the description of the stagnation points with the associated angle φ and $S_d = \left| \overrightarrow{S_1 S_2} \right|$ the stagnation separation. (b) Loosely confined case with $H = 8.78\,W$.

FIG. 8.   (a) $\tilde{J}/\nabla T$ as a function of channel width, H. (b) Stagnation angle φ and distance S_d/W as a function of H. (c) Velocity profiles along the channel direction v_x in the axis perpendicular to the channel and exactly in between two pillars [$A - A'$ in Fig. 7(a)], for various channel widths, shown as a polynomial fit to the data. s is the distance to the middle of the channel. (d) v_x profile in an axis parallel to the walls crossing the middle of the pillar [$B - B'$ in Fig. 7(a)], as a function of r, the separation to the obstacle center.

the pillar surface increases. This is similar to the flow for a fixed phoretic colloid and has the same origin. Deviations from this behavior are due to the confinement.

We have analyzed the dependence of the channel width for just one parameter set and fixed interfacial properties; we expect almost identical behaviors for other relevant parameter sets, although the exact location of the optimal channel width, here $H/W \approx 7.3$, could eventually vary.

2. Interobstacle separation effect.

In the limit of vanishing separation between obstacles, there is no expected net flux generated by the micropump; in the complementary limit, one single pillar is not able to create a considerable flux in an arbitrary long channel. To most precisely understand the transition between these limits, simulations at various pillar separations have been carried out. Figure 9 shows that the relevance of the vortex area and the tortuosity of the streamlines decrease with increasing obstacle separation. This can be understood since the flow field in the most immediate proximity of the obstacle has an intensity and direction determined by the surface rod properties, while the flow slightly farther away from the rod just needs to adapt to the given boundary conditions.

Decreasing the pillar separation importantly distorts the vortex areas, such that the counter-rotating flow becomes relatively more important. Therefore, the net flux importantly decreases for small (but not vanishing) pillar separation reaching a vanishing value as shown in Fig. 9(a) or even negative as shown in Figs. 9(b) and 10(a). Increasing obstacle separation increases the flux (see Fig. 2), until a maximum value is obtained ($D/W \approx 7$, for the parameters here employed), as shown in Fig. 10(a). Increasing the

where there can even be a residual flow in the opposite direction. The velocity profile along the middle axis parallel to the walls is shown in Fig. 8(d). The flow field in the most immediate proximity of the pillar can be understood as determined by the intrinsic obstacle properties and only weakly modified by the boundary conditions. The velocity profiles in Fig. 8(d) show a $1/r$ decay as the distance from
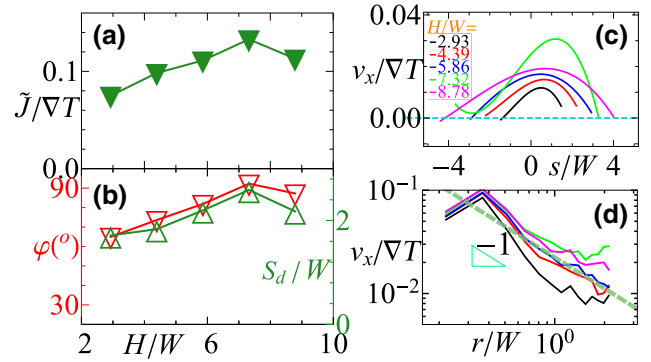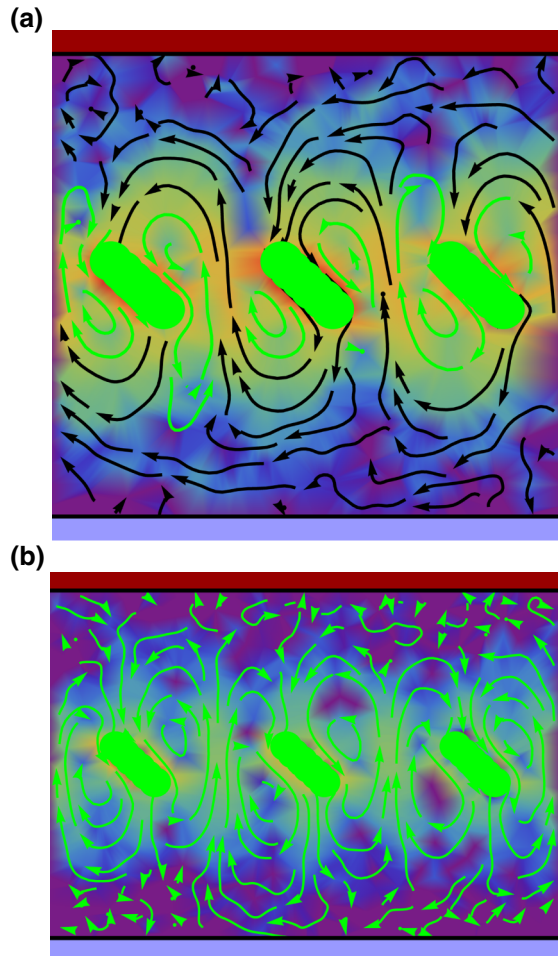
(a)

(b)

FIG. 9.   Flow pattern variation with very small obstacle separation D. (a) Vanishing flux case for $D = 1.95W$. (b) Reversed flux case for $D = 1.46W$.

FIG. 10.   (a) $\tilde{J}/\nabla T$ dependence with obstacle interseparation distance D. (b) Corresponding φ and S_d as a function of D. (c),(d) Velocity profiles, similar to Figs. 8(c) and 8(d).

micropump is intrinsically nonparabolic; see, for example, Fig. 2. The observed close-to-parabolic profiles occur just in the perpendicular axis, in between the pillars for intermediate separations.

The flow parallel to the walls at the center of the channel is shown in Fig. 10(d), where the flow field in the most immediate proximity of the obstacle shows a bit stronger dependence with D than with H in Fig. 8(d), but with similar $1/r$ decay. Note that the velocity profiles for the smallest interobstacle separation deviate from the $1/r$ decay scenario since their effective flow patterns are too strongly distorted.

3. The role of the obstacle aspect ratio.

As already described for the case of rodlike colloids [44], the anisotropic thermophoretic factor of elongated obstacles is expected to increase linearly with the aspect

separation further than this optimal value makes the flux decrease, but interestingly, this decay occurs very slowly. In this way, for the case with the largest separation where simulation has been performed here ($D/W \approx 18$), the total flux is just 50% smaller than that with the optimal separation. This result can be practically advantageous since devices with a smaller number of pillars will typically be easier and therefore cheaper to produce.

The location of the vortices' centers, which can be inferred from φ and S_d in Fig. 10(b), changes with increasing obstacle separation until they reach a stable location. This location no longer depends on D and seems therefore to be determined by the value of the channel width. The velocity profiles in the cross section in between the pillars is shown in Fig. 10(c) for various D values. The profiles are naturally related to their fluxes, such that small separations show flat profiles that can be on average negative, vanishing, or positive, while larger separations show progressively more paraboliclike profiles slightly tilted toward the pillar direction. Note that the flow induced by this
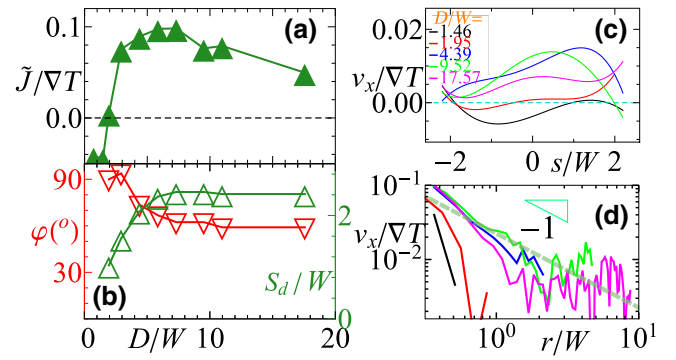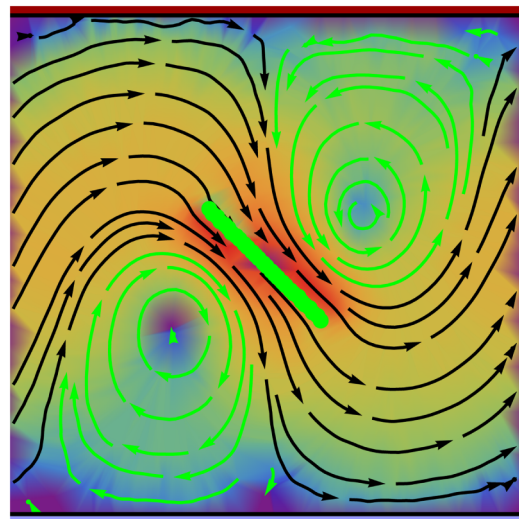

FIG. 11.   Flow streamlines in a microchannel with an obstacle with large aspect ratio, $W/d \simeq 11$.
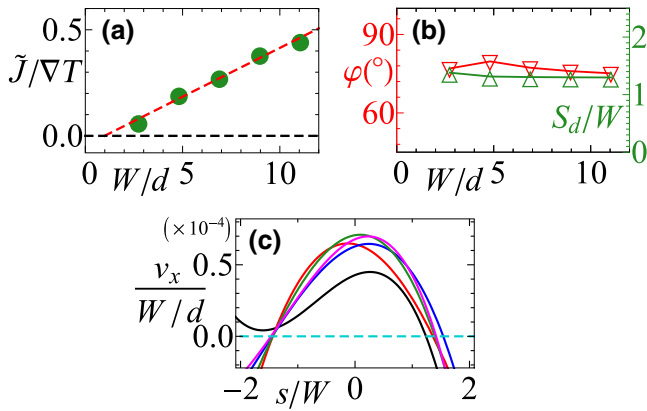
FIG. 12. (a) $\tilde{J}/\nabla T$ as a function of aspect ratio W/d. (b) Stagnation angle φ and distance S_d as a function of W/d. (c) Normalized velocity profile v_x at the cross section in between obstacles.

ratio and, therefore, the driving force along the channel for the anisotropic thermophoretic pump here investigated. In order to investigate the effect of the aspect ratio and reasonably decouple it from the other geometrical effects, we perform simulations varying the channel width and interpillar separation by keeping fixed ratios, $D/W = 2.93$ and $H = D$, and varying the wall temperatures to fix $\nabla T = 0.0105$. Figure 11 shows the flow streamlines for the largest aspect ratio here investigated, which can be compared with the streamlines of a smaller aspect ratio in Fig. 2. Interestingly, the flow patterns are very similar, which verifies that the shape of the flow streamlines is determined by the ratios D/W and H/D.

The measured normalized averaged flux in Fig. 12(a) very nicely shows a linear increase with W/d. Moreover, this similarity can be inferred also from the constant stagnation angle φ as well as the rescaled stagnation distance S_d/W for different aspect ratios in Fig. 12(b). The flow velocity profiles $v_x(z)$ perpendicular to the walls normalized by W/d collapse with a small deviation at the smallest aspect ratio, as shown in Fig. 12(c). This linear behavior implies that even with a small aspect ratio, we still obtain the same features of the study on the flow patterns and the averaged flux $\tilde{J}$.

C. Mapping to physical units

In order to provide an estimation of the actual pumping capability under experimental conditions of the proposed microfluidic device, we need to map the simulation units of the MPC model to those of real physical systems. We employ a similar strategy as the one introduced in Ref. [14], where three relevant MPC quantities are matched to real physical units. Very reasonable choices are to match the average MPC temperature T to 300 K and the mass density of the solvent to the density of water, 10^3 kg/m^3. The choice for the length scale is, however, much more arbitrary, but we can make a realistic choice of channel widths between 20 and 100 μm. This allows us to identify $\sqrt{k_B T/m}$ and, therefore, the typical velocities in this work to be in the order of 5 to 50 μm/s, which are competitive for the design of microfluidic devices. Furthermore, higher velocities could be reached since Fig. 12 shows that the velocity linearly increases with the obstacle aspect ratio, given that the ratio of channel width to obtacle length H/W and, more importantly, the temperature gradient ∇T are kept constant. On the other hand, it should be considered that the mesoscopic nature of the solvent makes it impossible to simultaneously match all the relevant physical quantities. In this way, with the above parameter choices, we provide a reasonable match to the ratio $\alpha_T \nabla T/\eta$, although not to each of the involved quantities. It is also very important that most parameters employed in the simulations are chosen due to computational efficiency, which is not related to any limitation of the physical phenomenon. Thus, simulations of larger systems, with smaller ∇T and larger α_T, are in principle possible, although not really meaningful at this stage. In this sense, the above dimensions should only be taken as an educated guess, with other sizes and velocities possible as well, in particular, considering the variaty of properties depending on the employed materials and system conditions.

IV. ALTERNATIVE SETUPS

The simulations presented in this work have so far considered only straight microchannels with fixed obstacles placed equidistant from the walls. There are, however,
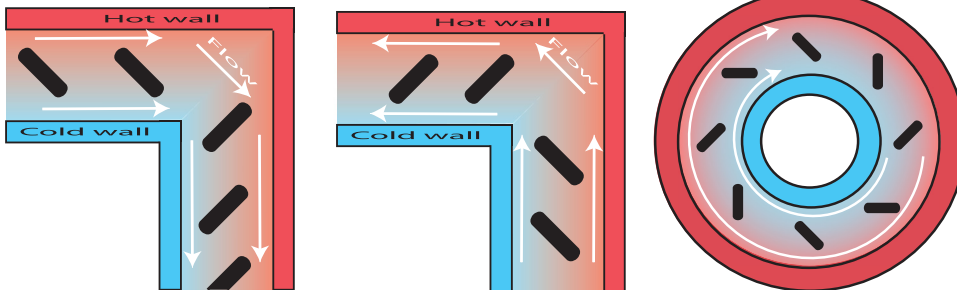

FIG. 13. Sketches of nonstraight channel configurations for anisotropic pumps, with the pillars kept at tilted orientations with respect to the walls. Note that, although the flux direction here corresponds to $\chi_T > 0$, the reverse direction is also possible by modifying the material properties.
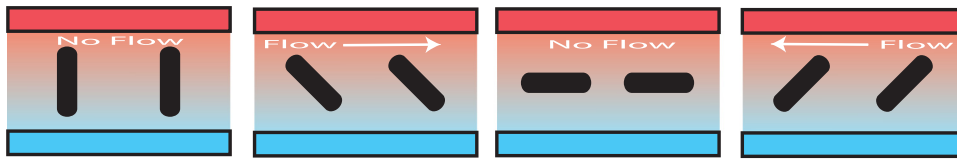
FIG. 14.   Sketch of the four consecutive configurations of a generator of alternating flow, in which states of no-flow and flow with positive and negative directions can periodically alternate.

no restrictions for building functional microfluidic devices based on the anisotropic thermophoretic effect. In the case that the pillars are not placed equidistant from the walls, the fluid streams with a nonsymmetric pattern, but in general the net fluid flux remains. In the limiting situation in which the obstacles are in contact with one of the walls, the system is similar in spirit to the phoretic ratcheted microchannels [14,68], where a net flux with a shearlike velocity profile is generated. The channels do not need to be straight either, and corners or curved geometries, as those shown in Fig. 13, do not hinder the fluid motion when the pillars are kept at the pertinent tilted orientation with respect to the walls. This is particularly important for microfluidic applications of this phenomena, since it shows that implementation in arbitrary geometries is possible.

Other interesting applications of the anisotropic phoretic effect in microfluidics are fluid mixers and generators of alternating flow. Fluid mixers can be obtained by building microchannels with elongated pillars fixed in the middle of the channel with a fixed angle, but with alternating positive and negative orientation, which would be adopting a type of "w" or symmetric saw disposition. In this case, types of Rayleigh-Bernard counter-rotating vortices are induced with sizes determined by the obstacles positions and rotating velocities given by the temperature gradients and the thermophoretic pillar properties. When two fluids converge into the phoretic micropump with anisotropic obstacles, the mixing is highly enhanced due to the intricate shape of the fluid flow; see, for example, Figs. 6(b) or 9(b). For mixing fluids [9,69–71], the pillars can, but do not need to be elongated, and no particular orientation is necessary.

The last structure that we discuss here is the generators of alternating flow, which emulates in some sense the alternating current of electromagnetic devices. The idea is to change the orientation of the pillars with time according to a prescribed protocol. This could be realized if movable obstacles could be engineered or, more realistically, by employing suspended elongated particles with fixed centers of mass and orientations externally controlled by the use of, for example, laser tweezers or rotating magnetic fields. It is straightforward to predict that if the obstacle orientation changes periodically with respect to the channel walls, the net flux will change as indicated in Fig. 14, from significant in one direction, to canceling, to significant in the opposite direction, and then vanishing again.

An example of systems that could be employed for this purpose are magnetizable particles in a nonmagnetic fluid, which in the presence of an external rotating magnetic field rotate with a constant frequency [72]. Although no simulation results are presented for the structures discussed in this section, the extensive results presented in the previous section serve as a strong proof of concept. This effect can be used not only as a flow alternator, but for example also as a flow switch.

V. CONCLUSIONS

We propose a strategy to design microfluidic devices based on anisotropic phoresis that use the asymmetric response of elongated objects to externally applied gradients, depending on their relative orientation.

The magnitude of the flow is determined by the phoretic properties of the pillar surfaces and also by the channel's geometric properties. We show that this design can facilitate the tunability of flow velocity and pattern by solely altering the orientation, aspect ratio, rugosity, or phoretic affinity (thermophobic or thermophilic) of the obstacles inside the same microchannel. The flux naturally increases with the obstacle aspect ratio and it is directly proportional to the pillar phoretic anisotropic factor. This means that the flux direction is not dictated by the thermophilic or thermophobic character of the surface, but by the anisotropic thermophoretic factor, which also depends, for example, on the surface properties, such as rugosity [44]. This might be counterintuitive, but it also provides the devices with an additional degree of versatility. Interestingly, the current device uses anisotropic pillars at the mid-channel, with an orientation that could eventually be manipulated by, for instance, optical tweezers. This might inspire a new avenue of microfluidic fabrication, such as fluidic switches, mixers, or flow alternators.

The required temperature differences can be experimentally obtained in two fundamentally different ways. One is by laser illumination when one of the wall surfaces is metal coated [39,43]. Such optical heating can be flexibly and remotely controlled in a very precise and programmable manner, and this microscale optical control can certainly find applications in optofluidics [36]. Alternatively, the microchannel walls can be in contact with heat reservoirs at different temperatures [34,73]. This contact heating can profit from existing residual heat flux, which

would eventually allow these devices to harvest part of the waste heat. Moreover, the proposed device can facilitate the cooling down of microscale heat sources, such as microelectronic chips. Furthermore, the current micropump needs only the presence of the walls and a simple fluid, but it will also be effective in the presence of a multicomponent fluid in a single phase or in a multiphase situation, where the pillars could interact with interfaces.

Although the micropumps here proposed have not yet been practically realized, various existing experimental results can serve as a proof of concept. An example is the osmotic flow, which has been shown to be responsible for the formation of $2D$ thermophoretic colloidal crystals close to a substrate [73,74]. Such flow produces an intercolloidal attraction, which maintains the colloidal assembly only in the presence of a temperature gradient. A different example can be found in the experimental results of a self-thermocapillary asymmetric gear [43], showing that a gear with an outer radius of 8 μm can rotate with a maximum angular velocity of 30 rad/s when externally heated.

The discussion performed in this work focuses on the thermophoretic case, but very importantly, all our arguments can be straightforwardly generalized to other phoretic effects, such as diffusiophoresis or electrophoresis. This is, for example, the case of a concentration gradient produced if one of the confining walls has a catalytic character. Simulation results have already demonstrated anisotropic diffusiophoresis [46], as well as the conceptual equivalence of, for example, the thermophoretic gear [41] and the catalytic counterpart [42]. Based on this principle, a proof of concept has also been experimentally achieved for catalytic self-electrophoretic microrotors [75], which show how platinum microgears in solutions of hydrogen peroxide with an outer radius of approximately 6 μm can rotate with a maximum angular velocity of 1.5 rad/s. The mechanisms of the phoretic microgears and ratcheted pumps [14,68] are different, but also closely related with the basic principle discussed in this work, what strongly supports the experimental feasibility of the devices proposed here in both their thermal and catalytic versions.

[1] G. M. Whitesides, The origins and the future of microfluidics, Nature **442**, 368 (2006).

[2] I. A. Martinez, E. Roldan, L. Dinis, and R. A. Rica, Colloidal heat engines: A review, Soft Matter **13**, 22 (2017).

[3] A. Nisar, N. Afzulpurkar, B. Mahaisavariya, and A. Tuantranont, Mems-based micropumps in drug delivery and biomedical applications, Sens. Actuators B **130**, 917 (2008).

[4] S. Herrlich, S. Spieth, S. Messner, and R. Zengerle, Osmotic micropumps for drug delivery, Adv. Drug Delivery Rev. **64**, 1617 (2012).

[5] Y.-N. Wang and L.-M. Fu, Micropumps and biomedical applications – a review, Microelectron. Eng. **195**, 121 (2018).

[6] F. Amirouche, Y. Zhou, and T. Johnson, Current micropump technologies and their biomedical applications, Microsyst. Technol. **15**, 647 (2009).

[7] C. K. Byun, K. Abi-Samra, Y.-K. Cho, and S. Takayama, Pumps for microfluidic cell culture, Electrophoresis **35**, 245 (2013).

[8] T. M. Squires and Stephen R. Quake, Microfluidics: Fluid physics at the nanoliter scale, Rev. Mod. Phys. **77**, 977 (2005).

[9] H. A. Stone, A. D. Stroock, and A. Ajdari, Engineering flows in small devices: Microfluidics toward a lab-on-a-chip, Annu. Rev. Fluid Mech. **36**, 381 (2004).

[10] A. A. Darhuber and S. M. Troian, Principles of microfluidic actuation by modulation of surface stresses, Annu. Rev. Fluid Mech. **37**, 425 (2005).

[11] J. Dauparas, D. Das, and E. Lauga, Helicalmicropumps near surfaces, Biomicrofluidics **12**, 014108 (2018).

[12] C. Zhou, H. Zhang, Z. Li, and W. Wang, Chemistry pumps: A review of chemically powered micropumps, Lab Chip **16**, 1797 (2016).

[13] S. Michelin, T. D. Montenegro-Johnson, G. DeCanio, N. Lobato-Dauzier, and E. Lauga, Geometric pumping in autophoretic channels, Soft Matter **11**, 5804 (2015).

[14] M. Yang and M. Ripoll, Thermoosmotic microfluidics, Soft Matter **12**, 8564 (2016).

[15] W. F. Paxton, K. C. Kistler, C. C. Olmeda, A. Sen, S. K. St Angelo, Y. Cao, T. E. Mallouk, P. E. Lammert, and V. H. Crespi, Catalytic nanomotors: Autonomous movement of striped nanorods, J. Am. Chem. Soc. **126**, 13424 (2004).

[16] E. L. Jewell, W. Wang, and T. E. Mallouk, Catalytically driven assembly of trisegmented metallic nanorods and polystyrene tracer particles, Soft Matter **12**, 2501 (2016).

[17] J. L. Anderson, Colloid transport by interfacial forces, Annu. Rev. Fluid Mech. **21**, 61 (1989).

[18] J. L. Moran and J. D. Posner, Phoretic self-propulsion, Annu. Rev. Fluid Mech. **49**, 511 (2017).

[19] A. Würger, Thermal non-equilibrium transport in colloids, Rep. Prog. Phys. **73**, 126601 (2010).

[20] R. Piazza and A. Parola, Thermophoresis in colloidal suspensions, J. Phys.: Condens. Matter **20**, 153102 (2008).

[21] R. Ganti, Y. Liu, and D. Frenkel, Molecular Simulation of Thermo-Osmotic Slip, Phys. Rev. Lett. **119**, 038002 (2017).

[22] L. Fu, S. Merabia, and L. Joly, What Controls Thermo-Osmosis? Molecular Simulations Show the Critical Role of Interfacial Hydrodynamics, Phys. Rev. Lett. **119**, 214501 (2017).

[23] B. V. Derjaguin, G. Sidorenkov, E. Zubashchenko, and E. Kiseleva, Kinetic phenomena in the boundary layers of liquids 1. The capillary osmosis, Prog. Surf. Sci. **43**, 138 (1993).

[24] J. F. Brady, Particle motion driven by solute gradients with application to autonomous motion: Continuum and colloidal perspectives, J. Fluid Mech. **667**, 216 (2011).

[25] J. R. Howse, R. A. L. Jones, A. J. Ryan, T. Gough, R. Vafabakhsh, and R. Golestanian, Self-Motile Colloidal Particles: From Directed Propulsion to Random Walk, Phys. Rev. Lett. **99**, 048102 (2007).

[26] D. A. Saville, Electrokinetic effects with small particles, Annu. Rev. Fluid Mech. **9**, 321 (1977).

[27] T. N. Shendruk, O. A. Hickey, G. W. Slater, and J. L. Harden, Electrophoresis: When hydrodynamics matter, Curr. Opin. Colloid Interface Sci. **17**, 74 (2012).

[28] O. A. Hickey, T. N. Shendruk, James L. Harden, and G. W. Slater, Simulations of Free-Solution Electrophoresis of Polyelectrolytes with a Finite Debye Length using the Debye-hückel Approximation, Phys. Rev. Lett. **109**, 098302 (2012).

[29] W. F. Paxton, P. T. Baker, T. R. Kline, Y. Wang, T. E. Mallouk, and A. Sen, Catalytically induced electrokinetics for motors and micropumps, J. Am. Chem. Soc. **128**, 14881 (2006).

[30] S. Sengupta, D. Patra, I. Ortiz-Rivera, A. Agrawal, S. Shklyaev, K. K. Dey, U. Córdova-Figueroa, T. E. Mallouk, and A. Sen, Self-powered enzyme micropumps, Nat. Chem. **6**, 415 (2014).

[31] I. Ortiz-Rivera, H. Shum, A. Agrawal, A. Sen, and A. C. Balazs, Convective flow reversal in self-powered enzyme micropumps, Proc. Natl. Acad. Sci. **113**, 2585 (2016).

[32] S. Das, O. E. Shklyaev, A. Altemose, H. Shum, I. Ortiz-Rivera, L. Valdez, T. E. Mallouk, A. C Balazs, and A. Sen, Harnessing catalytic pumps for directional delivery of microparticles in microchambers, Nat. Com. **8**, 14384 (2017).

[33] S. Duhr, S. Arduini, and D. Braun, Thermophoresis of DNA determined by microfluidic fluorescence, Eur. Phys. J. E **15**, 277 (2004).

[34] D. Vigolo, R. Rusconi, H. A. Stone, and R. Piazza, Thermophoresis: Microfluidics characterization and separation, Soft Matter **6**, 3489 (2010).

[35] T. Tsuji, K. Kozai, H. Ishino, and S. Kawano, Direct observations of thermophoresis in microfluidic systems, Micro. Nano. Lett. **12**, 520 (2017).

[36] D. Baigl, Photo-actuation of liquids for light-driven microfluidics: State of the art and perspectives, Lab Chip **12**, 3637 (2012).

[37] K. Namura, K. Nakajima, and M. Suzuki, Quasi-stokeslet induced by thermoplasmonic marangoni effect around a water vapor microbubble, Sci. Rep. **7**, 45776 (2017).

[38] T. R. Kline, W. F. Paxton, Y. Wang, D. Velegol, T. E. Mallouk, and A. Sen, Catalytic micropumps: Microscopic

convective fluid flow and pattern formation, J. Am. Chem. Soc. **127**, 17150 (2005).

[39] H.-R. Jiang, N. Yoshinaga, and M. Sano, Active Motion of a Janus Particle by Self-Thermophoresis in a Defocused Laser Beam, Phys. Rev. Lett. **105**, 268302 (2010).

[40] C. Liu and Z. Li, Molecular Dynamics Simulation of Composite Nanochannels as Nanopumps Driven by Symmetric Temperature Gradients, Phys. Rev. Lett. **105**, 174501 (2010).

[41] M. Yang and M. Ripoll, A self-propelled thermophoretic microgear, Soft Matter **10**, 1006 (2014).

[42] M. Yang, M. Ripoll, and K. Chen, Catalytic microrotor driven by geometrical asymmetry, J. Chem. Phys. **142**, 054902 (2015).

[43] C. Maggi, F. Saglimbeni, M. Dipalo, F. De Angelis, and R. Di Leonardo, Micromotors with asymmetric shape that efficiently convert light into work by thermocapillary effects, Nat. Commun. **6**, 7855 (2015).

[44] Z. Tan, M. Yang, and M. Ripoll, Anisotropic thermophoresis, Soft Matter **13**, 7283 (2017).

[45] M. Yang, R. Liu, M. Ripoll, and K. Chen, A microscale thermophoretic turbine driven by external diffusive heat flux, Nanoscale **6**, 13550 (2014).

[46] M. Yang, R. Liu, M. Ripoll, and K. Chen, A microscale turbine driven by diffusive mass flux, Lab Chip **15**, 3912 (2015).

[47] M. Tasinkevych, M. G. Campbell, and I. I. Smalyukh, Splitting, linking, knotting, and solitonic escape of topological defects in nematic drops with handles, P. Natl. Acad. Sci. **111**, 16268 (2014).

[48] Q. Liu, B. Senyuk, M. Tasinkevych, and I. I. Smalyukh, Nematic liquid crystal boojums with handles on colloidal handlebodies, P. Natl. Acad. Sci. **110**, 9231 (2013).

[49] A. Malevanets and R. Kapral, Mesoscopic model for solvent dynamics, J. Chem. Phys. **110**, 8605 (1999).

[50] A. Malevanets and R. Kapral, Solute molecular dynamics in a mesoscale solvent, J. Chem. Phys. **112**, 7260 (2000).

[51] R. Kapral, Multiparticle collision dynamics: Simulation of complex systems on mesoscales, Adv. Polym. Sci. **140**, 89 (2008).

[52] G. Gompper, T. Ihle, D. M. Kroll, and R. G. Winkler, English Multi-particle collision dynamics: A particle-based mesoscale simulation approach to the hydrodynamics of complex fluids, Adv. Polym. Sci. **221**, 1 (2009).

[53] T. Ihle and D. M. Kroll, Stochastic rotation dynamics: A galilean-invariant mesoscopic model for fluid flow, Phys. Rev. E **63**, 020201 (2001).

[54] T. Ihle and D. M. Kroll, Stochastic rotation dynamics. II. Transport coefficients, numerics, and long-time tails, Phys. Rev. E **67**, 066706 (2003).

[55] E. Tüzel, T. Ihle, and D. M. Kroll, Dynamic correlations in stochastic rotation dynamics, Phys. Rev. E **74**, 056702 (2006).

[56] M. Ripoll, K. Mussawisade, R. G. Winkler, and G. Gompper, Dynamic regimes of fluids simulated by multiparticle-collision dynamics, Phys. Rev. E **72**, 016701 (2005).

[57] M. Ripoll, K. Mussawisade, R. G. Winkler, and G. Gompper, Low-reynolds-number hydrodynamics of complex fluids by multi-particle-collision dynamics, Europhys. Lett. **68**, 106 (2004).

[58] D. Lüsebrink and M. Ripoll, Temperature inhomogeneities simulated with multiparticle-collision dynamics, J. Chem. Phys. **136,** 084106 (2012).

[59] M. Yang and M. Ripoll, Thermophoretically induced flow field around a colloidal particle, Soft Matter **9,** 4661 (2013).

[60] M. Gustav, Zur kinetischen theorie der einatomigen körper, Ann. Phys. **316,** 657 (1903).

[61] D. Lüsebrink, M. Yang, and M. Ripoll, Thermophoresis of colloids by mesoscale simulations, J. Phys.: Condensed Matter **24,** 284132 (2012).

[62] J. D. Weeks, D. Chandler, and H. C. Andersen, Role of repulsive forces in determining the equilibrium structure of simple liquids, J. Chem. Phys. **54,** 5237 (1971).

[63] M. Yang and M. Ripoll, Driving forces and polymer hydrodynamics in the soret effect, J. Phys.: Condens. Matter **24,** 195101 (2012).

[64] M. Yang and M. Ripoll, Drift velocity in non-isothermal inhomogeneous systems, J. Chem. Phys. **136,** 204508 (2012).

[65] Z. Tan, Ph.D. thesis, School Universitätzu Köln, 2018.

[66] J. Burelbach, D. B. Brueckner, D. Frenkel, and E. Eiser, Thermophoretic forces on a mesoscopic scale, Soft Matter **14,** 7446 (2018).

[67] C.-C. Huang, G. Gompper, and R. G. Winkler, Hydrodynamic correlations in multiparticle collision dynamics fluids, Phys. Rev. E **86,** 056711 (2012).

[68] M. Shen, F. Ye, R. Liu, K. Chen, M. Yang, and M. Ripoll, Chemically driven fluid transport in long microchannels, J. Chem. Phys. **145,** 124119 (2016).

[69] A. Marin, M. Rossi, B. Rallabandi, C. Wang, S. Hilgenfeldt, and C. J. Kähler, Three-Dimensional Phenomena in Microbubble Acoustic Streaming, Phys. Rev. Appl. **3,** 041001 (2015).

[70] B. Rallabandi, A. Marin, M. Rossi, C. J. Kähler, and S. Hilgenfeldt, Three-dimensional streaming flow in confined geometries, J. Fluid. Mech. **777,** 408 (2015).

[71] R. H. Liu, J. Yang, M. Z. Pindera, M. Athavale, and P. Grodzinski, Bubble-induced acoustic micromixing, Lab Chip **2,** 151 (2002).

[72] S. Melle, O. G. Calderón, M. A. Rubio, and G. G. Fuller, Microstructure evolution in magnetorheological suspensions governed by mason number, Phys. Rev. E **68,** 041503 (2003).

[73] F. M. Weinert and D. Braun, Observation of Slip Flow in Thermophoresis, Phys. Rev. Lett. **101,** 168301 (2008).

[74] R. Di Leonardo, F. Ianni, and G. Ruocco, Colloidal attraction induced by a temperature gradient, Langmuir **25,** 4247 (2009).

[75] A. M. Brooks, M. Tasinkevych, S. Sabrina, D. Velegol, A. Sen, and K. J. M. Bishop, Shape-directed rotation of homogeneous micromotors via catalytic self-electrophoresis, Nat. Commun. **10,** 495 (2019).